Research Paper

A statistical approach to understand the role of inclusions on the fatigue resistance of superelastic Nitinol wire and tubing

Scott W. Robertson[a,*], Maximilien Launey[b], Oren Shelley[c], Ich Ong[d], Lot Vien[d], Karthike Senthilnathan[d], Payman Saffari[e], Scott Schlegel[f], Alan R. Pelton[g]

[a]Fathom Engineering, 600 Addison Street, Berkeley, CA 94710, USA
[b]Glassimetal Technology, Inc., 2670 E Walnut Street, Pasadena, CA 91107, USA
[c]Medina Medical, 937 Hamilton Avenue, Menlo Park, CA 94025, USA
[d]Nitinol Devices & Components (NDC), 47533 Westinghouse Dr, Fremont, CA 94539, USA
[e]Endologix, 2 Musick Road, Irvine, CA 92618, USA
[f]ATI Wah Chang, 1600 Old Salem Road NE, Albany, OR 97321, USA
[g]G. RAU Inc., 704 Rancho Arroyo Parkway, Fremont, CA 94536, USA

ABSTRACT

Superelastic wires and diamond-shaped stent surrogates were manufactured from Nitinol rods and tubing, respectively, from five different mill product suppliers – Standard VAR, Standard VIM, Standard VIM+VAR, Process-Optimized VIM+VAR, and High-Purity VAR. High-cycle fatigue tests up to 10^7 cycles were conducted under tension–tension conditions for wires and bending conditions for diamonds. These materials were compared under both testing methods at 37 °C with 6% prestrain and 3% mean strain (unloading plateau) with a range of alternating strains. The High-Purity VAR material outperformed all alloys tested with a measured 10^7-fatigue alternating strain limit of 0.32% for wire and 1.75% for diamonds. Process-Optimized VIM+VAR material was only slightly inferior to the High Purity VAR with a diamond alternating bending strain limit of 1.5%. These two "second generation" Nitinol alloys demonstrated approximately a $2\times$ increase in 10^7-cycle fatigue strain limit compared to all of the Standard-grade Nitinol alloys (VAR, VIM, and VIM+VAR) that demonstrated virtually indistinguishable fatigue performance. This statistically-significant increase in fatigue resistance in the contemporary alloys is ascribed to smaller inclusions in the Process-Optimized VIM+VAR material, and both smaller and fewer inclusions in the High-Purity VAR Nitinol.

© 2015 Elsevier Ltd. All rights reserved.

*Corresponding author. Tel.: +1 415 682 4445.
  E-mail address: scott@fathomengineering.com (S.W. Robertson).

1.   Introduction

The detriment of chemical impurities on the fatigue resistance of biomedical materials is well documented. For example, the high-purity composition of extra low interstitials (ELI) Ti–4Al–6V ELI covered by ASTM F136 has become the preferred version for fatigue- and fracture-critical medical implant applications (ASTM F136-13, 2013). Similarly, in recent years, the effects of impurities, primarily C and O, that may form non-metallic inclusions (NMIs), in biomedical-grade NiTi (Nitinol) have been studied. In particular, investigations have demonstrated fatigue crack nucleation in Nitinol from NMIs (and/or voids) in the simple raw material form (Wick et al., 2004; Schaffer and Plumley, 2009; Rahim et al., 2013), surrogate medical device implant fatigue specimens (Tolomeo et al., 2000; Pelton, 2008; Robertson and Ritchie, 2008; Gall et al., 2008; Lin et al., 2011, 2012; Pike et al., 2011; Robertson et al., 2012; Pelton et al., 2008), and even finished commercial devices (Pelton et al., 2008; Hull and Robertson, 2009). On a commercial scale, Nitinol is melted by vacuum arc remelting (VAR), vacuum induction melting (VIM) or a combination of the two. The purity of the raw materials, combined with these different melting techniques leads to variations in the size, abundance, and chemical composition of NMI's. Consequently, it is difficult to ascertain the most promising route for improvements in fatigue behavior of Nitinol medical devices without extensive studies.

The industry standard for acceptable NMI limits in Nitinol materials governs the maximum NMI length and area fraction (ASTM F2063-12, 2012). While, these are important parameters that influences fatigue resistance, there are other variables with potentially equal or greater importance. Specifically, to fully evaluate the fatigue resistance of Nitinol we subdivided the possible contributing variables into three distinct categories:

1) Stress-concentrations: microscale phenomena that locally elevate the stress levels, thereby promoting the nucleation of a fatigue crack.
   L_{max}=maximum inclusion length in the drawing direction
   L_{median}=median inclusion length in the drawing direction
   L_{mean}=mean inclusion length in the drawing direction
   G=grain size
   a=surface defect size, e.g. scratch or gouge depth
2) Probabilistic considerations: variables that increase the likelihood of stress concentration residing in a susceptible region of the device that would prematurely nucleate a fatigue crack.
   A=total area fraction of inclusions measured in percent
   ρ=density of inclusions measured in number of inclusions per unit area or unit volume
3) Macro-mechanics: variables governing the overall stress or strain state of the specimen
   A_f=austenite finish temperature
   ϵ_a=strain amplitude
   ϵ_m=mean strain
   σ_U=upper plateau stress

σ_L=lower plateau stress
σ_H=stress hysteresis ($\sigma_U - \sigma_L$)
σ_Y=yield stress, as defined by a 0.2% offset line measured from the martensitic elastic loading portion of the stress–strain diagram

Manufacturing the specimens to have similar mechanical properties (σ_U, σ_L, σ_H, σ_Y), transformation temperature (A_f), surface smoothness (a), and grain sizes (G) allowed us to investigate in isolation the influence of the inclusion size (L_{max}, L_{median}, L_{mean}) and population distribution (A, ρ) on the fatigue resistance of Nitinol. However, it is difficult, if not impossible, to isolate the role of each of these variables to determine which, if any, is the dominant variable in improving fatigue resistance. Herein we present data comparing Nitinol with five different NMI-profiles to gain a deeper understanding of the role of each of these variables. Furthermore, this paper presents fatigue data on two forms of testing methodology: wire tension–tension fatigue and bending fatigue on laser-cut "diamond" surrogates from tubing. As such, this research provides the most comprehensive fatigue data on Nitinol with respect to composition and specimen form.

2.   Materials

Five unique materials were examined in this study: Standard VAR, Standard VIM+VAR, Standard VIM, Process-Optimized VIM+VAR, and High-Purity VAR. The designation "Standard" indicates that the material underwent conventional melting techniques with normal purity input raw materials. Two new grades of materials have recently become commercially available that we designated "Process-Optimized" and "High-Purity". The Process-Optimized material is manufactured using raw materials with purity levels comparable to Standard alloys, but the melting and solidification parameters have been optimized to minimize the NMI size. The High-Purity material is manufactured using superior input raw materials to limit both the abundance and size of inclusions. The exact manufacturing techniques for the melting, solidification, and primary conversion of these materials are proprietary trade secrets of each mill product supplier. The wrought material properties were reported by the mill product suppliers in accordance with ASTM F2063 and presented in Table 1 for both wire and tubing.

2.1.   Wires

Wires with unique NMI-profiles were selected to compare the effects of inclusion size, distribution, chemical composition, and area fraction (Table 1). Specifically:

Standard VAR – Nitinol melted using vacuum arc remelting (VAR) with conventional-purity raw materials.
Standard VIM+VAR – Nitinol first melted using vacuum induction melting (VIM) followed by VAR using conventional-purity raw materials.
High Purity VAR – Nitinol melted using VAR and ultra-high-purity raw materials.

Table 1 – Wrought material data for wire and tubes for chemical composition, transformation temperatures, and microstructure as reported by the mill product supplier and compared to the industry-accepted standard. Primary differences are shown by bold italic font. **Values that were not reported by the mill product supplier are listed as "NR".**

| | Product | Standard VAR | | Standard VIM+VAR | | Standard VIM | Process Optimized VIM+VAR | High Purity VAR | | ASTM F2063 (ASTM F2063-12) |
		Wire	Tube	Wire	Tube	Tube	Tube	Wire	Tube	
Chemical composition (wt%)	Nickel	55.91	55.83	55.95	55.89	55.8	55.98	55.8	56.1	54.5–57.0
	Titanium	Balance	Balance	Balance	Balance	Balance	Balance	Balance	Balance	Balance
	Oxygen+Nitrogen	0.0248	0.0274	0.0308	0.0197	0.041	0.026	0.006	0.0063	≤ 0.050
	Carbon	<0.0021	<0.0020	0.026	0.0268	0.033	0.0269	<0.0020	<0.0020	≤ 0.050
	Aluminum	<0.0050	<0.0050	<0.0100	NR	NR	NR	<0.0050	<0.0050	–
	Cobalt	<0.0050	<0.0050	<0.0100	<0.0100	0.003	<0.0100	<0.0050	0.03	≤ 0.050
	Copper	<0.0050	<0.0050	<0.0100	<0.0100	<0.0010	<0.0100	<0.0050	<0.0050	≤ 0.010
	Chromium	<0.0050	<0.0050	<0.0100	<0.0100	0.004	<0.0100	<0.0050	<0.0050	≤ 0.010
	Hydrogen	0.0013	0.0015	<0.0050	0.0008	0.0011	0.0007	0.0011	0.0008	–
	Iron	<0.0050	<0.0050	<0.0100	0.0062	0.011	0.011	<0.0050	0.0063	≤ 0.050
	Manganese	NR	<0.0050	NR	NR	NR	NR	<0.0050	<0.0050	–
	Molybdenum	NR	<0.0050	<0.0100	<0.0100	NR	<0.0100	<0.0050	<0.0050	–
	Niobium	<0.0050	<0.0050	<0.0100	<0.0100	<0.0010	<0.0100	<0.0050	<0.0050	≤ 0.025
	Silicon	NR	0.003	<0.0100	<0.0100	NR	<0.0100	<0.0025	<0.0025	–
	Sulfur	NR	<0.0010	<0.0100	<0.0100	NR	<0.0100	<0.0010	<0.0010	–
	Tin	NR	<0.0100	<0.0100	<0.0100	NR	<0.0100	<0.0100	<0.0100	–
	Tungsten	NR	<0.0050	<0.0100	<0.0100	NR	<0.0100	<0.0050	<0.0050	–
Transformation temperature*	A_f (°C)	1	−19	−5	−10	−1	−9	2	−9	–
Non-metallic inclusion/porosity	*Max. longitudinal length (mm)*	20	38	11	17	7	19	14	15	≤ 39
	Area fraction (%)	1.14	1.25	1.45	1.1	0.7	1.18	0.24	0.46	≤ 2.8

* Measured by Differential Scanning Calorimetry (DSC) in accordance with ASTM F2004 (ASTM F2004-05, 2005).

All wires were processed to achieve identical final super-elastic mechanical properties (upper and lower plateau stresses). They underwent final drawing at a single manufacturing plant (Nitinol Devices and Components, Fremont, CA, USA) using redraw material from three melting sources to eliminate the variable of wire drawing. The wires were drawn using a series of cold work and annealing passes eventually ending at a 0.229 mm diameter with $43\pm3\%$ cold work area reduction. The wires were then straightened on a strand annealing line at 505 °C for 10–15 s, then cut to individual lengths and further heat treated at 505 °C for 2–5 min to simulate a nominal stent shape-setting process. Finally, all wires were chemically etched and polished to remove thermal oxides and create a uniform, smooth surface; additionally, the grip sections of the wires were masked so that additional time in the chemical etch solution resulted in a reduced gauge section. The matching final austenite finish (A_f) transformation temperatures of 17 ± 3 °C were confirmed by the non-contact bend and free recovery method (ASTM F2082-06, 2006). Additionally, identical upper and lower plateau stress values were verified per ASTM F2516 (ASTM F2516-07e2, 2007) testing procedures (Fig. 1a).

2.2. Tubing

Five tube hollows ranging in starting size from 10.5 mm to 25.4 mm were procured from the various mill product suppliers and were manufactured to their finished dimensions, 8.0 mm outer diameter, 0.37 mm wall, at a single facility (G. Rau, GmbH, Pforzheim, Germany). All tubes were given the identical final drawing sequence to impart 30% cold work and subsequently straightened in a horizontal furnace. Processing parameters were chosen to achieve as close to identical superelastic mechanical properties as possible (upper and lower plateau stresses). Longitudinal metallographic cross-sections of the finished tubes were prepared and examined by scanning electron microscopy (JEOL Model 6360) for microstructural characterization using Image Pro Plus v. 7.0 (Media Cybernetics, Inc.).

The tubes were then laser cut into diamond-shaped stent surrogate pairs, stress relieved, and then expanded in two steps to their final shape (Fig. 2). Each diamond was subjected to a total of 10 min processing time at 505 °C, again at a single manufacturing facility (NDC, Fremont, CA, USA) to minimize process variability. All finished diamond-shaped specimens had an A_f temperature of 20 ± 3 °C as measured by the bend and free recovery method (ASTM F2082-06, 2006). Finally, the diamonds were etched in Kroll's $HF–HNO_3–H_2O$ solution to remove the thermal oxide layer and electropolished to eliminate surface blemishes that could prematurely nucleate fatigue cracks during the experiments. These chemical-processing steps targeted a total weight loss of 25% to ensure uniform surface smoothness and elimination of any heat affected zone created during the laser cutting operation.

3. Methods

3.1. Wire

To isolate the role of inclusions, the round wire samples were tested in tension–tension fatigue under simple mode-I
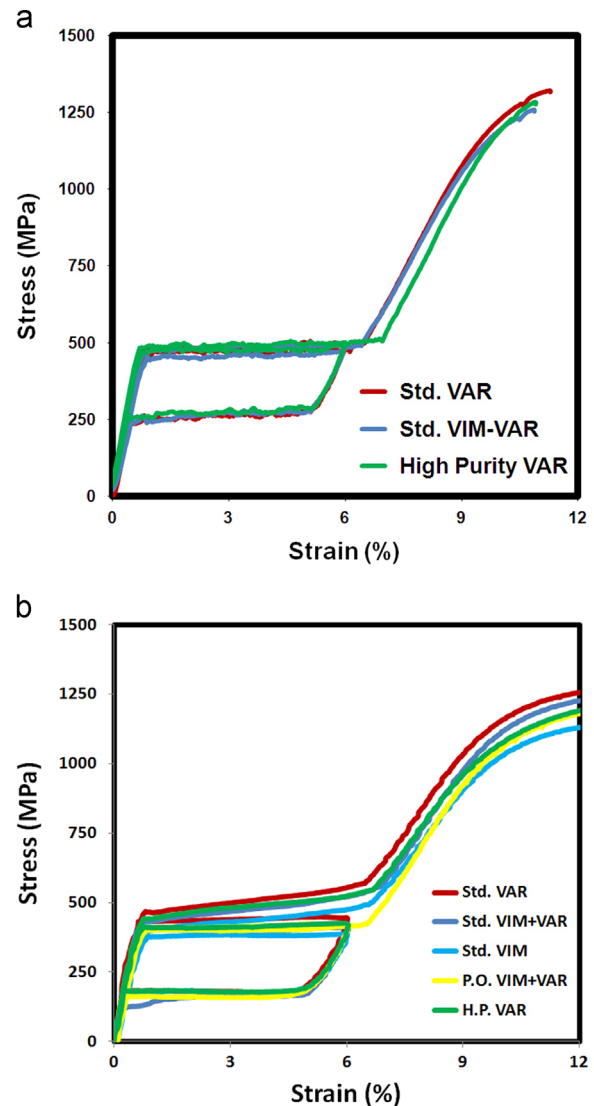

Fig. 1 – (a) Stress–strain diagram for the three alloy types for the wires that shows identical mechanical behavior in the 0–6% strain range. (b) Stress–strain diagram for the five alloy types from the tubes used for the diamond fatigue testing. Stress–strain diagram computed in accordance with ASTM F2516 (ASTM F2516-07e2, 2007) for the five alloy types showing similar, but not identical, mechanical behavior in the 0–6% strain range utilized in this fatigue study. The lower plateau stress values around which cycling was performed were more similar than the upper plateau stress values. The small differences amongst the samples are not expected to have a significant impact on the fatigue performance.

loading conditions. This method of loading imparts a uniform stress across the entire cross-section, thereby involving all inclusions within the gauge length rather than isolating only the near-surface inclusions or surface processing conditions that dominate rotary bend or stent-surrogate fatigue tests. Fatigue testing was performed using a 5-station Instron Model E3000 (each with isolated load cells for dynamically monitoring fracture) in 37 °C distilled water, at a frequency of 20 Hz, and under displacement-control conditions. Displacement–strain relationships were determined by conducting

simulated tests with a calibrated 3 mm gage extensometer (Epsilon Technology Corporation, Jackson, WY 83001). Wires were fatigued either until fracture occurred or 10^7 cycles was achieved without fracture.

Specimens were first strained to 6% to simulate stent constraint in a catheter, and then unloaded to 3% strain to simulate deployment into an undersized vessel. Strain amplitudes were varied between 0.18% and 0.50% with a minimum of four wires per type tested at each amplitude. Fractures that occurred at the grips were excluded from the data set, resulting in a total of 186 individual data points, with >50 per alloy type.

3.2. Tube

Unlike the tension–tension wire fatigue tests described above, the diamond bending fatigue tests underwent mixed mode loading conditions. Therefore, due to the complicated mechanics of the stent subcomponent surrogates, it was necessary to conduct sophisticated finite-element analyses (FEA) to characterize the localized stress–strain behavior correlated to input displacements (Fig. 3). The commercial FEA package ABAQUS (Standard version 6.2-1) was used in combination with the user-defined material subroutine (UMAT) Nitinol-3D version 4.1-2 for these computational
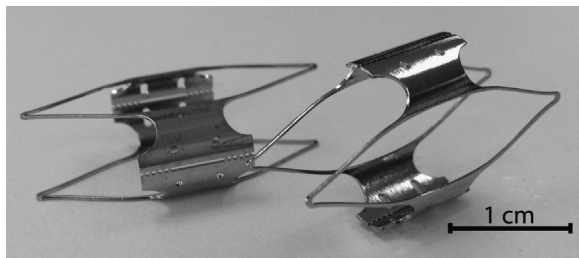

Fig. 2 – Test coupons were cut with the struts aligned parallel to the tubing longitudinal axis, then thermo-mechanically shape set to an open flat diamond configuration with inside dimensions of 7.00 mm height and 24.68 mm width. Strut widths were 0.30 mm except at the tips of the diamond where the dimension was increased to 0.46 mm. The pair was separated into an individual diamond specimen for the fatigue test.
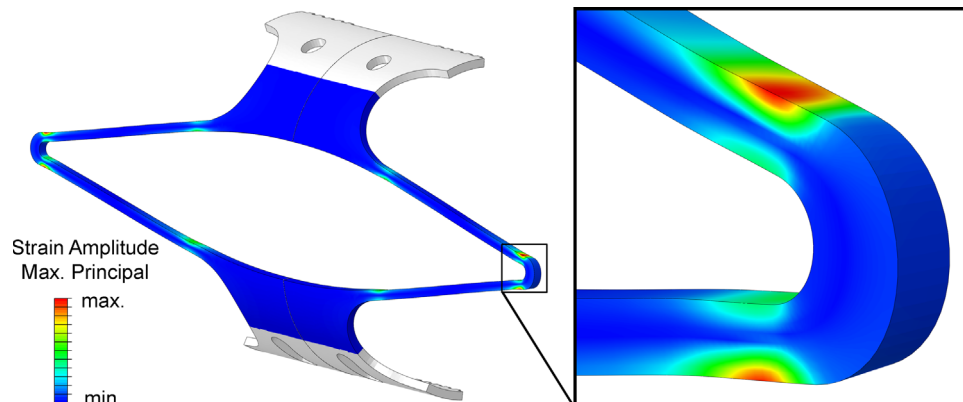
analyses. The non-linear mechanical properties for the Nitinol UMAT were derived from uniaxial tension tests conducted in accordance with ASTM F2516 using the same Nitinol tubes with identical thermal and surface treatment as those used for the diamond-shaped specimens. The displacements required to reach the desired pre-strain of 6% and mean strain of 3% were computed at cycle 1, whereas the displacement inputs to achieve the various strain amplitudes were computed at cycle 3 of the FEA analysis. This technique of utilizing computational modeling to establish experimental displacement inputs is common in the evaluation of Nitinol stent-like surrogates (Tolomeo et al., 2000; Pelton, 2008; Robertson and Ritchie, 2008; Gall et al., 2008; Lin et al., 2011, 2012; Pike et al., 2011; Robertson et al., 2012; Pelton et al., 2008).

Fatigue testing was performed using a 12-station Instron Model E3000 (each with isolated load cells for dynamically monitoring fracture) in 37 °C distilled water, at a frequency of 20 Hz, and under displacement-control conditions. Crosshead displacement pre-strained the specimens to 6% loading strain to simulate crimping into a catheter, unloaded to 3% strain to simulate deployment into an undersized vessel, and then cycled at strain amplitudes ranging from 0.41% to 2.33% with a minimum of 3 duplicate samples per strain amplitude condition. Specimens were cycled either until fracture occurred or 10^7 cycles was achieved without fracture. All fractures were examined and those originating either away from the FEA-identified high strain region (e.g. near the grips or mid-strut) or from processing defects (e.g. surface scratches) were excluded so as not to bias the data. This resulted in a total of 214 specimens that were included in the data, 117 of which resulted in fracture, and 97 of which survived to 10^7 cycles.

3.3. Data analysis methodology

To distinguish trends amongst the fatigue test data, logistic regression analyses were performed (Hosmer and Lemeshow, 1989). First, we defined a logarithmic failure thresholds of 10^7 cycles and assigned a value of 1 for a failure event and a value 0 for survival, thereby converting the raw fatigue data into a binary data set (Fig. 4a). Next, the binary data was combined for an average value for any data sets where some samples

Fig. 3 – Finite element model used to compute the global crosshead displacements required to achieve the desired mean and alternating strains at the "hotspot" regions of localized strain concentration near the apexes.

within the population survived and others fractured (Fig. 4b). In this form, the data was then fitted with a sigmoid curve (Fig. 4c) using a Logistic Response Function using the equation:

$$P = \exp(\mathbf{Q})/(1 + \exp(\mathbf{Q})) \tag{1}$$

$$\mathbf{Q} = \mathbf{x^T}\beta \tag{2}$$

within these equations, P is the probability of fracture at 10^7 cycles, $\mathbf{x}$ is a vector of strain amplitude values, and β is a vector of model coefficients. The overall statistical significance of the resulting curves was evaluated by a likelihood ratio test. Goodness of fit was assessed with the Hosmer–Lemeshow χ^2 statistic, with a significance level threshold set at $\alpha = 0.050$.

4. Results

4.1. Microstructural analysis

Statistical microstructural analysis was done on all three versions of the wire and five versions of the tubing. Here we concentrate on the microstructural analysis of the tubing, although similar trends were observed in the finished wire characterization. Fig. 5 shows representative micrographs of the finished tubes.

There exist several key differences among the five material types. Of the two Standard alloys, the VIM+VAR alloy has a smaller maximum inclusion length and greater inclusion area fraction compared to the VAR material. This smaller maximum and average inclusion length and larger area fraction results in a greater inclusion density in the VIM+VAR alloys compared to VAR materials. Both the Standard and High Purity VAR alloys are virtually carbon-free and thereby contain only Ti_4Ni_2O inclusions rather than a combination of Ti_4Ni_2O and TiC for VIM+VAR. To summarize, each material type is ranked (Table 2) to the multiple variables that were identified earlier.

Maximum inclusion size: PO VIM+VAR < (Std. VIM, High Purity VAR) < Std. VIM+VAR < Std. VAR

Average inclusion size: Std. VIM < PO VIM+VAR < Std. VIM+VAR < High Purity VAR < Std. VAR

Impurity concentration, (ppm Carbon): High Purity VAR = Std. VAR < (Std. VIM+VAR, Std. VIM, PO VIM+VAR)

Impurity concentration (ppm Oxygen): High Purity VAR < (Std. VAR, Std. VIM+VAR, Std. VIM, PO VIM+VAR)

Inclusion area fraction: High Purity VAR < (Std. VAR, Std. VIM+VAR, PO VIM+VAR) < Std. VIM

Inclusion density: High Purity VAR < Std. VAR < Std. VIM+VAR < PO VIM+VAR < Std. VIM

Comparison of the finished tube microstructure to the wrought material certified values reveals some interesting trends. First, the maximum inclusion length generally increases from wrought product to finished tube. This trend is expected because of the drawing process creating stringer-like defects as inclusions break into smaller fragments. Additionally, there is a trend for the area fraction of inclusions to increase. This difference cannot be attributed to void formation, which is common with stringer-type inclusions. Instead, the difference is ascribed to inclusion break-up and concentration into a smaller cross-sectional area such that they are more readily observed in all $500\times$ fields of view rather than dispersed over a larger wrought cross section.

While these differences from wrought product to finished form can certainly be explained as discussed above, there was a clear outlier in the data. Specifically, the difference between the wrought and finished tube reported values for the Standard VIM material was significantly different than all other materials. Whereas the difference in total area fraction was < 0.5% in all other materials, the Standard VIM material showed a 2% increase from wrought to finished tube. Likewise, the maximum inclusion length in the finished tube was 7-times longer than reported in the wrought product, whereas all other materials showed less than $5\times$ increase. Without any scientific rationale for these significant differences, we opine that the methodology employed by the Standard VIM mill product supplier to characterize and certify the material differs significantly from the other melting partners. This conclusion highlights the importance of uniformity in measurement technique before comparing certified NMI data amongst suppliers.

Examining the maximum, mean, and median inclusion lengths in isolation does not fully characterize the real non-Gaussian distribution of NMIs in these materials. Instead, a histogram of the distribution of NMI sizes is a more complete representation. If one considers the distribution as a percentage (Fig. 6a), a clear trend of shorter length inclusions in the Process Optimized VIM+VAR material is observed relative to all other materials. Since fatigue is a probabilistic phenomenon influenced by the total number of potential nucleation sites, it is equally important to evaluate the distribution of NMIs from an absolute density (number of inclusions per unit area) perspective
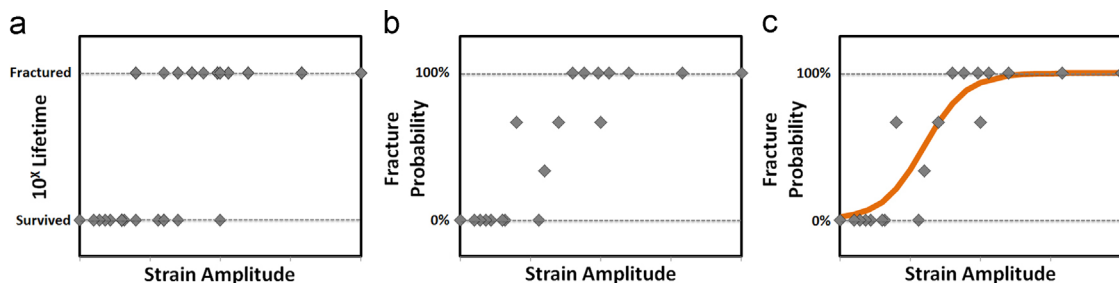

Fig. 4 – Procedures for logistic regression analysis by (a) plotting data in a binary manner at a fixed 10^7 lifetime as either fractured or survived, (b) combining overlapping data and changing the binary data into probability, then finally (c) fitting the data with a sigmoidal curve.
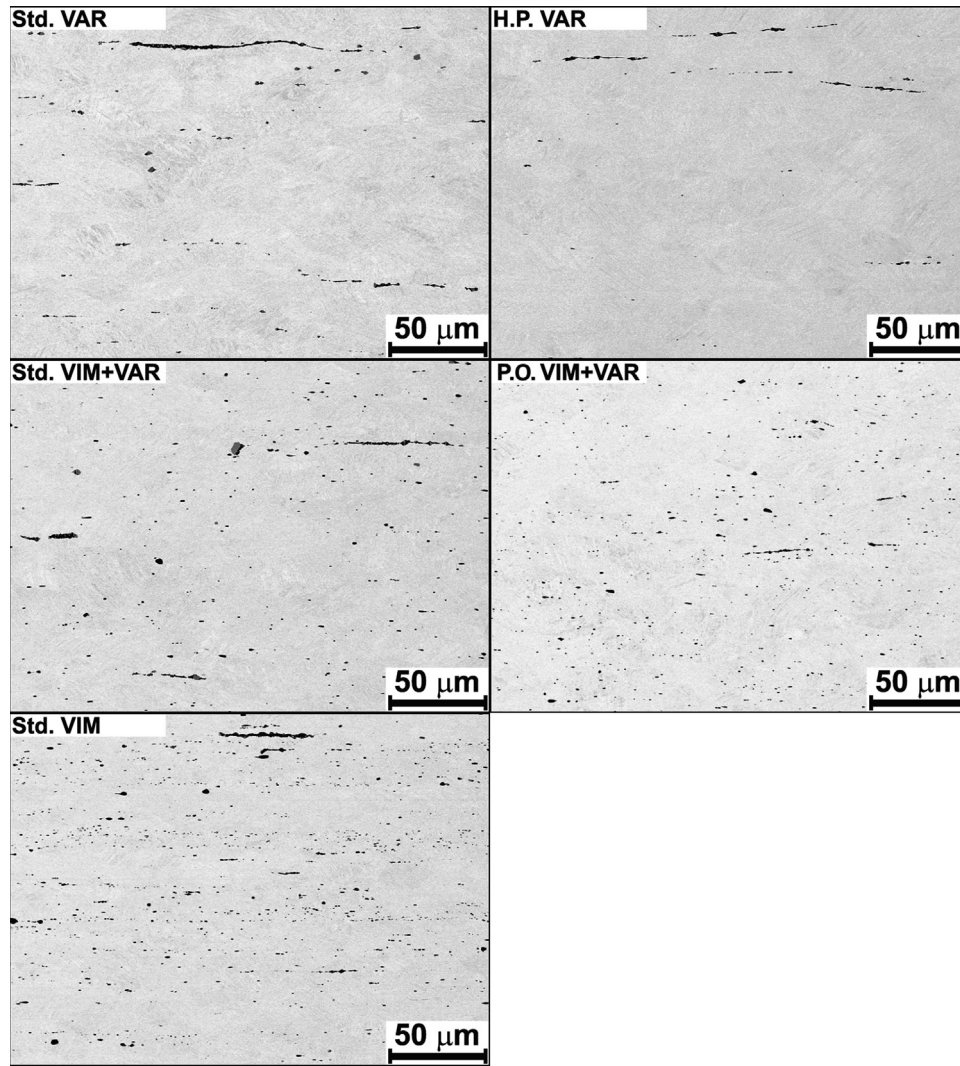
Fig. 5 – Representative backscatter electron micrographs of the five finished tubes. Note the increasing area fraction, and decreasing inclusion size, from top to bottom in the Standard grade materials. The High-Purity VAR material demonstrated reduction of size, area fraction, and density of NMIs, whereas the Process-Optimized VIM+VAR showed only a reduction of size.

Table 2 – Finished tubing microstructural characterization as quantified using a standardized metallographic technique from a single metallurgical laboratory to eliminate cross-laboratory bias.						
		Standard VAR	Standard VIM+VAR	Standard VIM	Process Optimized VIM+VAR	High Purity VAR
Non-metallic inclusion dimensions* (µm)	L_{max}	101	81	50	20	40
	L_{mean}	3.55	1.86	1.29	1.40	2.88
	L_{median}	1.72	1.23	1.06	1.06	1.26
Area fraction (%)	NMI	1.46	1.51	2.67	1.49	0.41
	porosity	0.12	0.05	0.05	0.01	0.02
	Total	1.58	1.55	2.72	1.50	0.43
Other	NMI density, #/mm^2	3247	7272	21,483	12,702	1425
	Average grain size (µm)	14	17	12	14	17

* Measured longitudinally at a magnification of $500\times$ per ASTM F2063 with three fields of view for a total of $\sim 0.1\ mm^2$ area surveyed.
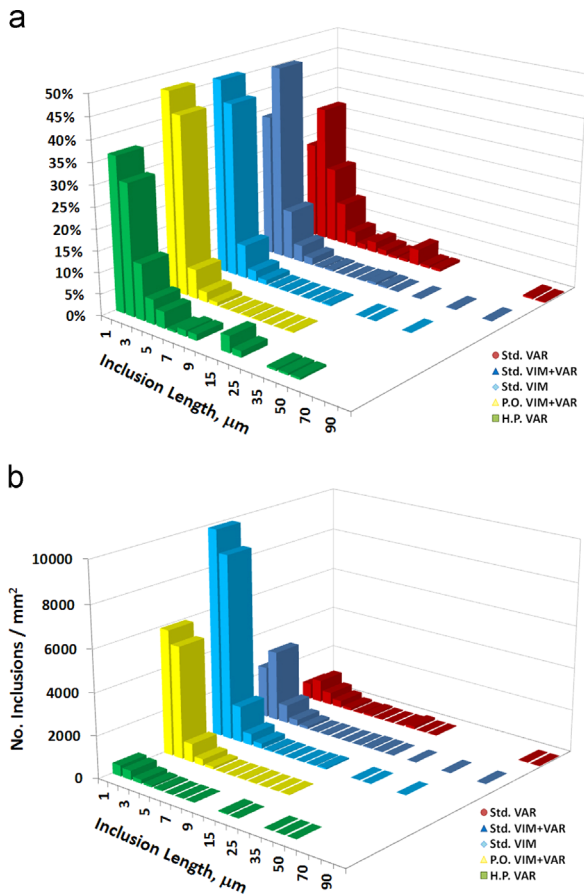
Fig. 6 – Histogram of NMI length distributions in each of the five finished 8 mm diameter tubes plotted versus (a) total percentage of all inclusions within a given specimen, and (b) absolute count, or density, of inclusions. Note the resolution limit of detection is 0.59 μm, below which the NMI's were excluded from the count.
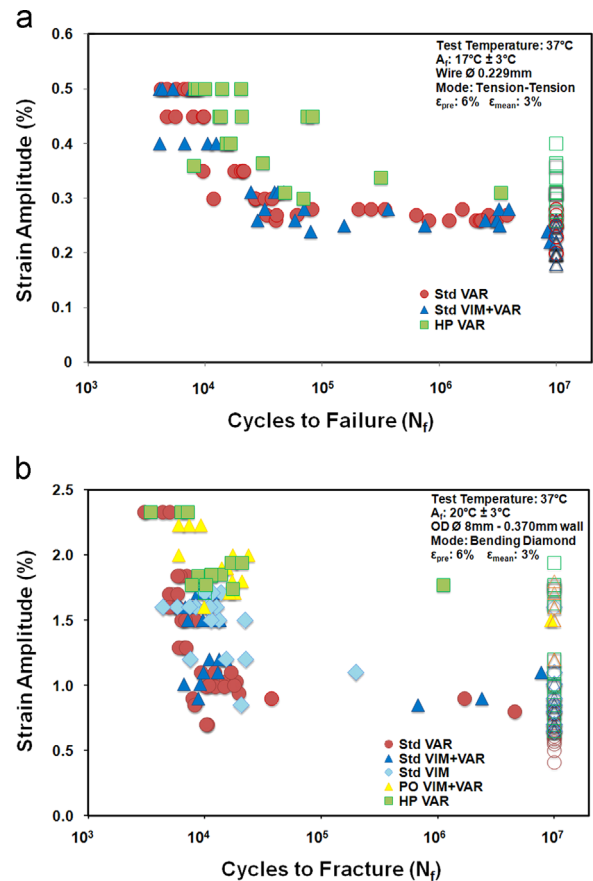

Fig. 7 – (a) Strain-Life plot for the three versions of Nitinol wire that shows the 186 individual fracture and survival data points. (b) Strain-Life plot showing the individual fracture and survival data points for each of the five alloys evaluated by diamond fatigue. Filled data points signify fracture, whereas open data points represent sample survival at 10^7 cycles.

too. Fig. 6b shows that all of the VIM melted materials have significantly more inclusions than the VAR-only melted materials. This is not surprising, since the VIM melting process introduces titanium–carbide (TiC) inclusions in addition to oxide inclusions that are present in all Nitinol materials.

4.2. Wire fatigue

The wire fatigue data are plotted in Fig. 7a using a conventional Nitinol Strain-Life diagram. All three of the materials demonstrate similar low cycle-high strain amplitude behavior (N~10^4 cycles) between approximately 0.3 and 0.5% strain amplitude. At lower strain amplitudes, the number of cycles to fracture increases, typical of fatigue behavior of engineering materials. The two Standard alloys demonstrate virtually identical fatigue performance, with a 10^7-cycle fatigue strain limit of ~0.25%. Furthermore, the data within a given strain amplitude were very consistent; that is, all of the specimens either fractured or all survived at a fixed strain amplitude. Conversely, the High Purity VAR material exhibited a noticeably greater 10^7 fatigue endurance limit of ~0.32%. Also unlike the Standard alloys, the High Purity VAR material exhibited a more varied fracture profile. Specifically, at many strain amplitudes some High

Purity wires would fracture early while others would survive to 10^7 cycles.

4.3. Diamond fatigue

Fatigue data are plotted in Fig. 7b using a conventional Nitinol Strain-Life diagram. In the low cycle fatigue range, i. e. at and below 10^4 cycles, all five alloys have comparable performance greater than approximately 1.5% strain amplitude. This result is not surprising since low-cycle, high-amplitude fatigue is dominated by the elevated stress intensity resulting from high strain amplitudes much more so than the influence of microstructural disturbances.

Conversely, there are observable differences in the high cycle (>10^5) fatigue performance. Specifically, if we define the 10^7-fatigue strain limit as the strain below which all samples survived 10^7 cycles, there exists a minor separation between the Standard VAR (0.6%) and the Standard VIM+VAR and Standard VIM (both at 0.8%). These data are consistent with the previously reported literature measuring the fatigue performance of other diamond-shaped stent surrogates made from Standard material at 3% mean strain (Pelton et al., 2008). The

Table 3 – Summary of 10^7-cycle fatigue strain limits for the wires and diamonds for each source material.

	Standard VAR		Standard VIM+VAR		Standard VIM		Process Optimized VIM+VAR		High Purity VAR	
	Wire	Tube	Wire	Tube	Wire	Tube	Wire	Tube	Wire	Tube
10^7-cycle fatigue strain amplitude (%)	0.25	0.6	0.25	0.8	n/a	0.8	n/a	1.50	0.32	1.75

Process-Optimized VIM+VAR and High-Purity VAR materials each demonstrate marked improvement in the high cycle fatigue resistance, demonstrating a 10^7-cycle fatigue strain limit of 1.50% and 1.75%, respectively, which is approximately a two-fold improvement compared to the Standard alloys.

5. Discussion

The trends in fatigue limit at 10^7 cycles for the various Nitinol compositions are comparable between the two testing methods, albeit with greater strain amplitude ranges for the diamond fatigue testing in bending. The resultant 10^7-cycle fatigue strain amplitudes for each material and test method are summarized in Table 3. The difference between uniaxial and bending fatigue behavior is well known and speaks to the difference in volume of stressed material with each cycle. Macherauch (2002) summarized the general effects of deformation mode on fatigue life of engineering materials and showed that uniaxial conditions lead to the shortest lives compared with bending fatigue or rotary beam fatigue test conditions. It is interesting, though that the differences between wire and bending data for the three materials were not consistent. For example, the two Standard wire materials have a 10^7-cycle limit of 0.25%, whereas the VIM+VAR material had a greater (0.8%) strain limit than VAR (0.6%) under diamond bending conditions. This difference may provide insight into a secondary effect related to distribution of the carbides and oxides in the VIM+VAR material.

As mentioned in Section 4, the fatigue behavior of the standard materials was more consistent at all strain levels than with the High Purity VAR results. We hypothesize that this divergent fracture behavior in the High Purity VAR is due to the decreased probability of the sample containing an inclusion large enough to nucleate a fatigue crack. Employing a logistic regression probabilistic fatigue approach, as discussed previously (Hosmer and Lemeshow, 1989), we analyzed the data at fixed "fatigue-strain limit" conditions: 10^5, 10^6, and 10^7 cycles to test this hypothesis for the three Nitinol wires (Fig. 8) and 10^7 cycles for the five tubes (Fig. 9).

For the wire fatigue probability plots in Fig. 8, we combined the confidence bands of the two Standard alloys since they overlapped for the most part. Specifically, the probabilistic fatigue data show statistically indistinguishable high-cycle, >10^5, fatigue behavior between the two Standard alloys. Interestingly, the High Purity VAR material exhibited vastly superior fatigue resistance to both of Standard Nitinol alloy under both medium- and high-cycle fatigue conditions. Furthermore, the enhanced performance increases with increasing number of cycles as demonstrated by the widening gap between the confidence bands.

For the diamond fatigue probability plots in Fig. 9, we excluded the confidence bands for clarity. As with the wire, these diamond fatigue data demonstrated superior durability of the Process Optimized VIM+VAR and High Purity VAR materials compared to their Standard Nitinol counterparts.

The same logistical regression-fitting scheme described in Eq. (1) can be utilized to create a fitted predictive model that characterizes the exact contribution of each variable presented in the Introduction. Indeed, we expanded the variable vector **x** from Eq. (2) to include all measured variables discussed in Section 1, $x = <L_{max}, L_{median}, L_{mean}, G, a, A, \rho, A_f, \varepsilon_a, \varepsilon_m, \sigma_U, \sigma_L, \sigma_H, \sigma_Y>$. We then used the Minitab statistical software program to predict the corresponding best-fit vector of coefficients $\boldsymbol{\beta}$, plotted these predicted responses, and visually compare the predicted curves to the experimental curves in Fig. 9. With this approach, we were able to rank order the most important contributions from the characteristics of the inclusions.

We explored permutations of as few as two variables and as many as seven variables as simultaneous contributors to the fatigue behavior. The most convenient model to use would be one that leverages data that are already reported in most manufacturer's certificates of compliance – maximum inclusion length and area fraction measured on the wrought material per ASTM F2063. Unfortunately, using only those variables was insufficient to accurately predict the experimental data. Instead, the model that most accurately represented the experimental data interestingly contained only one stress-concentration variable (L_{max}), one probabilistic variable (ρ), and one macro-mechanics variable (ε_a). The predicted fracture probability curves that use the combined effect of these three variables is shown in Fig. 10 with the associated fitted predictive formula given as Eq. (3). Caution should be mentioned here that this predictive equation is valid only for this particular geometry, boundary conditions, and mechanical property tuning. Furthermore, importantly, the variables shown in Eq. (3) are measured on the *finished component*, not from the wrought product properties that are commonly reported.

$$\text{Prob. Fracture} = \frac{\exp(11.4\varepsilon_a + 0.154L_{max} + 2.12\ln(\rho) - 41.9)}{1 + \exp(11.4\varepsilon_a + 0.154L_{max} + 2.12\ln(\rho) - 41.9)}$$

(3)

By normalizing[1] each of the three variables for the five materials, the relative contribution of each variable was determined. Holding the strain amplitude fixed, since this is a boundary condition not an intrinsic material property, we computed that the maximum inclusion length has $4\times$ the

---

[1]Normalization was accomplished by centering each data set per $x'_i = (x_i - x_{ave})/(0.5 * x_{range})$.

influence on the fatigue resistance compared to the NMI density. This insight is important in driving the design of future fatigue resistance Nitinol alloys.

Statistical evaluation of the fatigue data provides further refinement in the fatigue performance differences amongst the five alloys. Depending upon the consequent severity that the fracture in a finished component has on the patient, most medical device failure mode and effect analyses allow no more than 5% fracture rate, with many products requiring <1%. At the conservative fracture rate of <1% (survival of 99%) there is no significant difference[2] amongst any of the three Standard alloys, which show 99% survival at strain amplitude values below 0.50%. Conversely, the High-Purity and Process-Optimized materials demonstrate a significant >2× improvement in survivable cyclic strain levels compared to Standard alloys. Specifically, the sigmoidal curves predict 99% survival at $\varepsilon_A \leq 1.40\%$ for the High-Purity VAR and $\varepsilon_A \leq 1.15\%$ for the Process-Optimized VIM+VAR. Despite a greater than 20% difference between these two alloys, there was a small overlap in confidence intervals between them, which does not allow us to conclude that these values have a statistically significantly difference.

Considering the more liberal acceptable fracture rate of 5% (i.e. 95% survival rate), there is a significant difference between the Standard VAR (0.58% strain amplitude) and the Standard VIM+VAR and Standard VIM that each accommodates 0.75% strain amplitude. Again, the High Purity materials demonstrated a significant ~2× increase in the allowable strain amplitude (1.33% for P.O. VIM+VAR and 1.55% for H.P. VAR) for 95% survival.

The power of this probabilistic evaluation of fatigue is evident if we combine observed clinical data with the fundamental material properties derived herein. For example (Fig. 11), if we take the observed clinical fracture rate of 43% after an average of 32 months in vivo (~5x10^6 walking cycles) from Nitinol stents implanted in the Femoral-Popliteal (Scheinert et al., 2005) and draw a horizontal line, we see that it crosses the Standard alloys used at the time of that study at a strain amplitude of ~0.8% at Point (a). Drawing a vertical line from that intersection point shows that the corresponding Nitinol stent manufactured from either High Purity VAR or Process Optimized VIM+VAR Nitinol is expected to have a fracture occurrence of <2% at Point (b).

6.   Limitations

Herein we presented fundamental material data and drew comparisons to finished products manufactured from those differing Nitinol melting techniques. However, there are a few key limitations that must be considered before adopting the information.

1) While the fatigue strain-life curves and consequent probability plots draw upon hundreds of individual data points, each

---

[2]True statistical significance cannot be determined using this technique. Sigmoidal curves are meant only to show trends. For the purposes of this analysis, we use the term "significant difference" to signify when the trendline of one data set resided outside of the upper 95th confidence interval of the data set being compared against.

set of specimens was manufactured from a single tubing lot (diamonds) or wire lot from a single melting campaign. Variations during melting or wire/tube manufacturing are possible, and may shift the experimental fatigue results from those observed herein. However, the trends were comparable to previously reported studies (Launey et al., 2014), thereby giving us good confidence in the data trends.

2) We were limited to alloy blends that were commercially available at the time of this investigation. That limitation forced the selection of starting materials with divergent wrought A_f temperatures. Specifically, the Standard VAR and the Standard VIM were approximately 10 °C colder and warmer, respectively, compared to the three other materials that all had $A_f \sim -10$ °C in the as-received form. The expected outcome of a 10 °C cooler A_f temperature is an increase in the plateau stress values and drop in fatigue resistance (Pelton et al., 2013). Conversely a 10 °C warmer A_f temperature is expected to result in a drop in plateau stress and increase in fatigue resistance. Taking this into account, it is reasonable to expect that the Standard VAR material would improve its fatigue resistance, and Standard VIM decrease its fatigue resistance, so that all three Standard alloys exhibit identical fatigue properties if the wrought A_f temperatures were identical.

3) Modification of shape-setting times/temperatures is an effective way to tune the transformation temperature of the finished product to limit the effects of the starting A_f. In this research, we held the processing times and temperatures identical to simulate a fixed manufacturing process regardless of the wire or tubing source. This practice resulted in reasonably similar finished specimen A_f of 17 ± 3 °C (wire) and 20 ± 3 °C (diamond). As shown in Fig. 1a, the wire mechanical properties were more consistent (upper and lower plateau stresses) than those from the tubing. Differences in mechanical properties can certainly influence the fatigue performance, although these small differences in the tubing are not expected to modify the trends. The upper and lower plateau stress values were within $\pm 5\%$ and $\pm 8\%$ of one another, respectively.

4) The pre-strain and mean-strain conditions provide just a single data point in the overall fatigue behavior profile of a Nitinol device. It is possible that changes to either variable may result in different fatigue behaviors. While it is expected that all five alloys would shift their fatigue resistance similarly with variations in these boundary conditions, a more complete study of their influence is warranted.

5) NMI size relative to specimen geometry was not studied. As the aspect ratio lessens (i.e. when the strut geometry gets nearer in size to the NMI dimensions) stress fields will rise and the fatigue resistance may fall accordingly.

6) Other research has highlighted that both NMI size and voids surrounding those NMIs are important parameters governing the fatigue life in research-grade ultrapure Nitinol (Rahim et al., 2013). For completeness, we quantify the NMI and porosity area fraction separately in Table 2. Comparisons between materials were performed using the combined total area fraction.

7) In order to establish probability plots with an acceptable goodness of fit, a tremendous number of samples must be tested. In the experiments reported herein, a minimum of 50
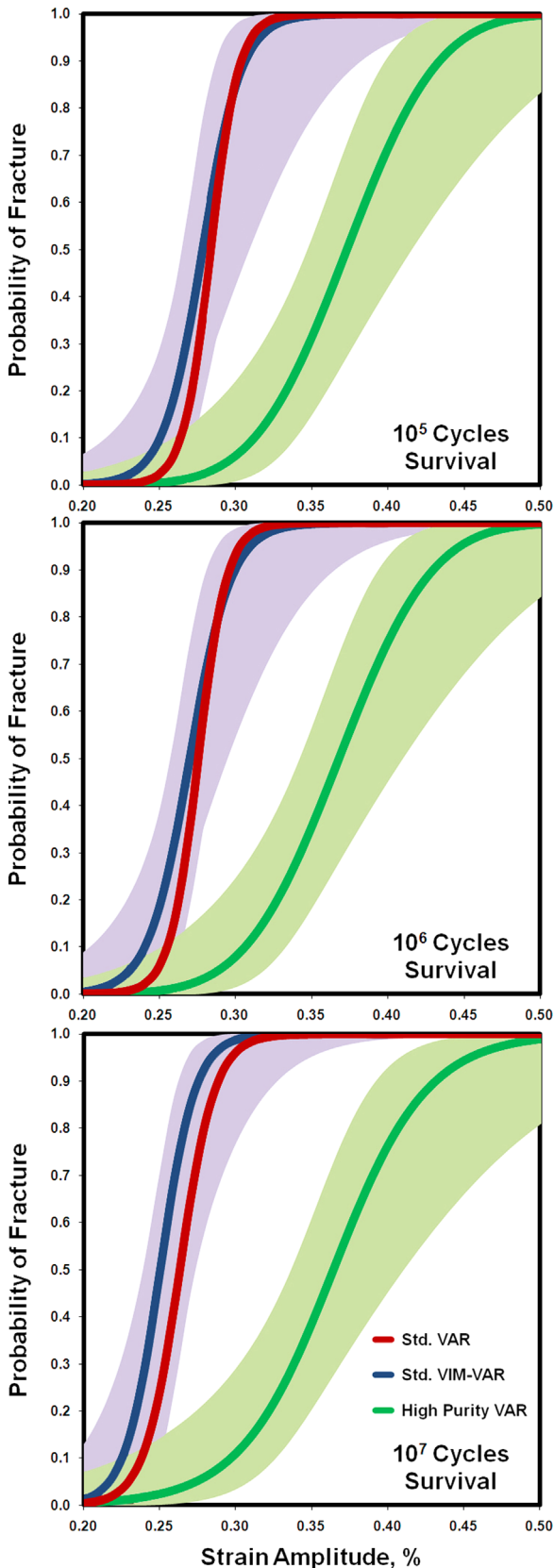
Fig. 8 – Probability of Nitinol wire fracture versus strain amplitude plots with the curve fit line shown bracketed by the 95th percentile upper and lower confidence interval bands.
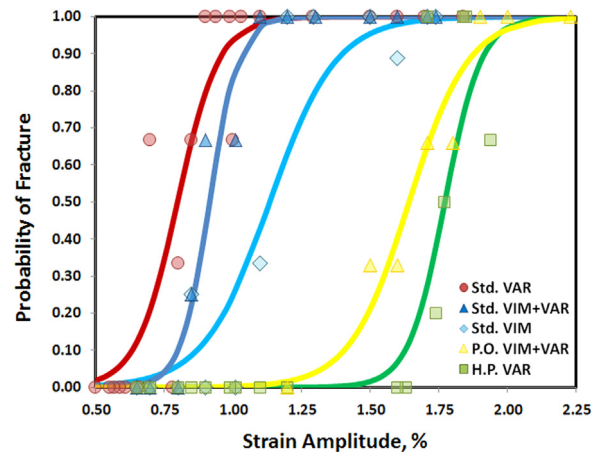

Fig. 9 – Probability of Nitinol diamond fracture at 10^7 cycles versus strain amplitude plots with a logit sigmoidal curve fit line for each data set.
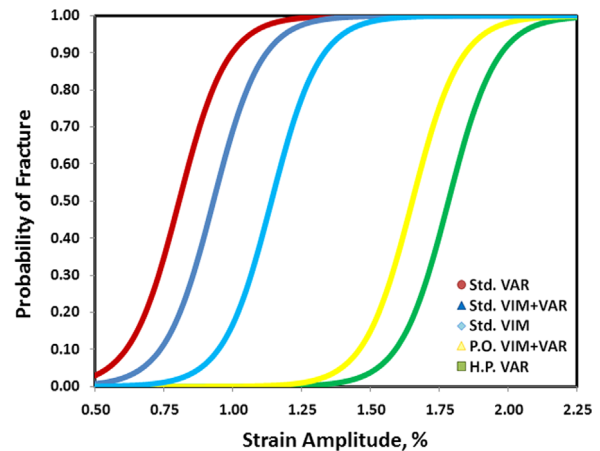

Fig. 10 – Fatigue fracture probability vs. strain amplitude plot predicted from Eq. (3), with general agreement to the experimentally-determined data in Fig. 9.

tests per material type were required. This large number of samples does increase the testing time and resources required to establish statistically-significant data.

8) Different product forms, dimensions, shape-setting schedules and complex loading modes are to be expected with commercial products. Consequently, the conclusions drawn herein using a single set of wire/tube dimensions and processing conditions may not apply to other Nitinol components that undergo a unique thermo-mechanical history.

7. Conclusions

Each of the alloys investigated in this study has a different inclusion-profile. Therefore, when that knowledge is combined with the probabilistic fatigue evaluation it provides us valuable insight on the role of the inclusions on fatigue
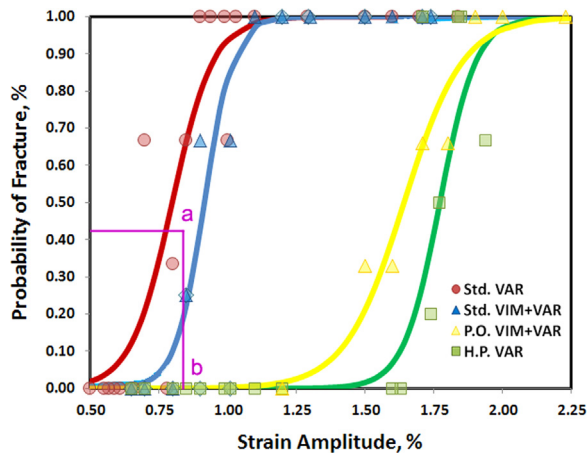
Fig. 11 – Demonstrated usage of the probabilistic fatigue data. Drawing a horizontal line corresponding to the clinically observed 43% fracture rate of Nitinol femoral-politeal-implanted stents (Scheinert et al., 2005), then drawing a corresponding vertical line from each intersection point suggests that the same stent made from either High Purity VAR or Process Optimized VIM+VAR Nitinol may demonstrate less than 2% fracture rates in vivo.

resistance of Nitinol.

1) Both a low-inclusion-density, larger inclusion size (Std. VAR) and a high-inclusion-density, smaller inclusion size (Std. VIM+VAR, and Std. VIM) material have statistically indifferent medium- and high-cycle ($>10^5$) fatigue performance. This observation suggests that both size (average and maximum) and the total number of inclusions are important variables in high-cycle fatigue resistance.

2) High Purity VAR material exhibits superior medium- and high-cycle fatigue resistance, with increasing divergence from Standard Nitinol with an increasing number of cycles. This observation suggests that the density of inclusions is the dominant variable governing high-cycle fatigue under these loading conditions and sample geometry. While not experimentally proven in Nitinol until now, this conclusion is unsurprising given the fact that high-cycle fatigue is a probability-driven phenomenon with crack nucleation occurring at low alternating strains only when a material "flaw" is located in a high stress/strain area of the sample.

3) Process Optimized VIM+VAR material also exhibits superior medium- and high-cycle fatigue resistance relative to Standard Nitinol. This observation suggests that the smaller maximum length of inclusions in this alloy is the dominating factor in its fatigue resistance.

4) Predictive modeling based upon the experimental fatigue data suggests that, under a constant pre-, mean-, and alternating-strain, that the fatigue resistance is due approximately 80% to the maximum inclusion length (L_{max}) and 20% to the inclusion density (ρ) in the finished product form (not the wrought certified values per ASTM F2063).

5) While the High Purity VAR and Process Optimized materials exhibit superior fatigue resistance over current

Standard alloys, these results suggest that an even more fatigue resistant Nitinol alloy could be achieved if melting practices could produce a low-inclusion-density, small-inclusion-size material.

R E F E R E N C E S

ASTM F136-13, Standard specification for wrought titanium–6aluminum–4vanadium ELI (Extra Low Interstitial) alloy for surgical implant applications (UNS R56401), Book of Standards Volume 13.01, Subcommittee F04.12, 2013.

ASTM F2004-05, Standard test method for transformation temperature of nickel–titanium alloys by thermal analysis, Book of Standards Volume 13.01, Subcommittee F04.15, 2005.

ASTM F2063-12, Standard specification for wrought nickel–titanium shape memory alloys for medical devices and surgical implants. ASTM Book of Standards Volume 13.01, Subcommittee F04.12, 2012.

ASTM F2082-06, Standard test method for determination of transformation temperature of nickel–titanium shape memory alloys by bend and free recovery, Book of Standards Volume 13.01, Subcommittee F04.15, 2006.

ASTM F2516-07e2, Standard test method for tension testing of nickel–titanium superelastic materials, ASTM Book of Standards Volume 13.2, Subcommmittee F04.15, 2007.

Gall, K., et al., 2008. Effect of microstructure on the fatigue of hot-rolled and cold-drawn NiTi shape memory alloys. Mater. Sci. Eng. A 486, 389–403.

Hosmer, D.W., Lemeshow, S., 1989. Applied Logistic Regression. John Wiley & Sons, New Jersey, USA.

Hull, J.E., Robertson, S.W., 2009. Bard recovery filter: evaluation and management of vena cava limb perforation, fracture, and migration. J. Vasc. Interv. Radiol. 20 (1), 52–60.

Launey, M., et al., 2014. Influence of microstructural purity on the bending fatigue behavior of VAR-melted superelastic Nitinol. J. Mech. Behav. Biomed. Mater. 34, 181–186.

Lin, Z., et al., 2011. Nitinol fatigue investigation on Stent-finish specimens using tension–tension method. J. Mater. Eng. Perform. 20, 591–596.

Lin, Z., et al., 2012. Nitinol fatigue life for variable strain amplitude fatigue. J. Mater. Eng. Perform. 21, 2628–2632.

Macherauch, E., 2002. Praktikum in Werkstoffkunde. Friedrich Vieweg & Sohn Verlagsgesellschaft mbH, Wiesbaden, Germany.

Pelton, A.R, 2011. Nitinol fatigue: a review of microstructures and mechanisms. J. Mech. Behav. Biomed. Mater. 20, 613–617.

Pelton, A.R., et al., 2008. Fatigue and durability of Nitinol stents. J. Mech. Behav. Biomed. Mater. 1, 153–164.

Pelton, A.R., et al., 2013. Rotary-bending fatigue characteristics of medical-grade Nitinol wire. J. Mech. Behav. Biomed. Mater. 27, 19–32.

Pike, K., et al., 2011. Development of the Z specimen for tensile–tensile, tensile–compression, compression–compression wire testing. J. Mater. Eng. Perform. 20, 835–837.

Rahim, M., et al., 2013. Impurity levels and fatigue lives of pseudoelastic NiTi shape memory alloys. Acta Mater. 61 (10), 3667–3686.

Robertson, S.W., Ritchie, R.O., 2008. A fracture-mechanics-based approach to fracture control in biomedical devices manufactured from superelastic Nitinol tube. J. Biomed. Mater. Res. B 84, 26–33.

Robertson, S.W., et al., 2012. Mechanical fatigue and fracture of Nitinol. Int. Mater. Rev. 57 (1), 1–37.

Schaffer, J.E., Plumley, D.L., 2009. Fatigue performance of Nitinol round wire with varying cold work reductions. J. Mater. Eng. Perform. 18, 563–568.

Scheinert, et al., 2005. Prevalence and clinical impact of stent fractures after femoropopliteal stenting. J. Am. Coll. Cardiol. 45 (2), 312–315.

Tolomeo, D., Davidson, S., Santinoranout, M., 2000. Cyclic properties of superelastic Nitinol: design implications. In: Proceedings of the International Conference on Shape Memory and Superelastic Technologies. SMST. Pacific Grove, CA, USA, pp. 409–417.

Wick, A., et al., 2004. Bending fatigue characteristics of Nitinol. In: Proceedings of the ASM Materials & Processes for Medical Devices Conference. Minneapolis, MN, USA. ASM International. pp. 15–20.